^{18}F-5-FPN: A Specific Probe for Monitoring Photothermal Therapy Response in Malignant Melanoma

Yichun Wang
  Union Hospital, Tongji Medical College, Huazhong University of Science and Technology

Mengting Li
  Union Hospital, Tongji Medical College, Huazhong University of Science and Technology

Wenxia Wang
  Union Hospital, Tongji Medical College, Huazhong University of Science and Technology

Hao Ji
  Union Hospital, Tongji Medical College, Huazhong University of Science and Technology

Chaoyi Jia
  The second Clinical Medical College, Tongji Medical College, Huazhong University of Science and Technology

Na Han
  Union Hospital, Tongji Medical College, Huazhong University of Science and Technology

Huiling Li
  Union Hospital, Tongji Medical College, Huazhong University of Science and Technology

Xiaodong Xu
  Unoin Hospital, Tongji Medical College, Huazhong University of Science and Technology

Honglin Jin
  Union Hospital, Tongji Medical College, Huazhong University of Science and technology

Yongxue Zhang
  Union Hospital, Tongji Medical College, Huazhog University of Science and Technology

Xiaoli Lan (✉ xiaoli_lan@hust.edu.cn)
  Union Hospital, Tongji Medical College, Huazhong University of Science and Technology

---

Abstract

Background

The increasing global burden and the significant breakthroughs in malignant melanoma therapy make urgent demands on efficient response evaluation and surveillance of adverse events. Though there have been a few probes explored for early diagnosis or staging of malignant melanoma, but rare for response assessment investigations except for common ^{18}F-deoxyglucose (^{18}F-FDG). Thus, this research would further explore the feasibility and ability of ^{18}F-5-fluoro-N-(2-(diethylamino)ethyl)picolinamide (^{18}F-5-FPN)PET imaging to evaluate photothermal therapy (PTT) response of malignant melanoma, simultaneously comparing with ^{18}F-FDG.

Methods

B16F10 and MDA-MB-231subcutaneous tumor models were irradiated with an 808 nm laser for PTT. ^{18}F-5-FPN and ^{18}F-FDG PET imaging were adopted to estimate the therapy response. B16F10, inflammatory, and MDA-MB-231 models were subjected to ^{18}F-FDG and ^{18}F-5-FPN PET static acquisitions and compared by quantitative data for assessing the specificity of different agents to different diseases. Furthermore, B16F10 and 231 models were exploited for survival analysis to observe the efficacy and response feature of PTT.

Results

Melanin in B16F10 tumors successfully transformed the optical energy into heat for PTT. H&E staining at 24 h discovered framework destruction of tumor tissue and extensive necrosis. The mean tumor uptakes of ^{18}F-5-FPN on Day 2 (7.52 ± 3.65%ID/g) and Day 6 (10.22 ± 6.00%ID/g) were much lower than before treatment (p < 0.01). However, no significant difference of the ^{18}F-FDG uptakes was found between Day 1 after PTT and before treatment. ^{18}F-5-FPN PET scanning only manifested B16F10 tumor strikingly, while they all accumulated ^{18}F-FDG highly. PTT contributed to suppressing B16F10 tumors' growth rapidly in a short time and prolonged the median survival of B16F10 models to some extent. Whereas, both of the temperature and growth of 231 tumors were not distinctly influenced.

Conclusions

Compared with ^{18}F-FDG PET scanning, ^{18}F-5-FPN PET imaging was capable of estimating PTT efficacy in malignant melanoma, successfully monitored the occult recurrence after therapy, and distinguished malignant melanoma from inflammation and other carcinomas well by high affinity to melanin. This

potential probe may provide a new approach for precise and useful response evaluation, timely therapeutic regimen management, and sensitive follow-up.

Background

Melanoma is an aggressive malignant skin neoplasm. Its global incidence is increasing, and Australasia, North America, and Europe are the regions with the highest incidence and mortality [1]. Currently, drug therapy of malignant melanoma (MM) has been expanded from conventional chemotherapy to targeted therapy and immunotherapy [2, 3]. Compared with the limited benefits of systemic chemotherapy, targeted therapy has a notable efficacy on the majority of patients with BRAF mutation. Immunotherapy resulted in better response than chemotherapy (26–40% vs. 4–14%) in a phase III randomized controlled trial [3–5]. However, drug resistance occurs in targeted therapy, and immunotherapy works slowly and triggers immune-related adverse events (rash, diarrhea, colitis, etc.) [4, 5]. The increasing global burden and intricate situation of novel therapies of MM make more urgent and stricter demands on efficient response evaluation.

Computed tomography (CT) and magnetic resonance imaging (MRI) are the most common techniques for therapy assessment in the clinic and the shrinkage of tumor size suggests a response. A typical response may present as an initial increase in size followed by regression later, i.e., "pseudoprogression" [6, 7]. Conventional imaging techniques have difficulty in distinguishing real progression from pseudoprogression. Immunotherapy usually takes a long time to observe a response, so that conventional imaging techniques cannot identify early responses, and repeated inspections are inevitable, prolonging the cycle of response evaluation [6, 8]. It is well-known that changes in function and metabolism always precede changes in tumor size. Functional imaging [such as positron-emission tomography (PET) imaging] is able to detect the early changes in the function and metabolism of tumors during treatment [7].

^{18}F-fluorodeoxyglucose (^{18}F-FDG) PET/CT imaging has a vital role in evaluating lesions' response to conventional chemotherapy but has limits for immunotherapy because the high glucose consumption of immune response may obscure the tumor response [8]. Both MM and inflammation accumulate ^{18}F-FDG, making it difficult to discriminate between pseudoprogression and real progression. One study utilized ^{18}F-FDG PET imaging to monitor the response of MM patients to anti-PD-1 therapy, finding that three out of eight cases of high uptakes were biopsy-confirmed inflammatory infiltration, and five were MM [9]. Therefore, more specific radiopharmaceuticals are needed for response evaluation [8].

Many agents, for example, ^{18}F-FBZA, 4-^{11}C-MBZA, ^{18}F-FPDA, ^{64}Cu-DOTA-NAPamide, and ^{68}Ga-TRAP(RGD)$_3$, have been explored for MM detection and staging [10]. Among them, ^{18}F-5-fluoro-N-(2-(diethylamino)ethyl)picolinamide (^{18}F-5-FPN), used in our previous studies, was shown to have high affinity for melanin and was quite promising for the early detection and precise staging of MM [11, 12]. Although some small molecule-based or peptide-based probes have been developed to diagnose MM early, few studies further estimated the utility of these potential agents in treatment response evaluation,

except for ^{18}F-FDG and ^{18}F-fluorothymidine (^{18}F-FLT) [6–8, 13, 14]. Thus, we sought to uncover the properties of ^{18}F-5-FPN in assessing MM's response to photothermal therapy (PTT).

PTT is a therapy that utilizes heat to eliminate tumor cells with laser light via photothermal conversion [15]. Melanin, usually abundant in MM, has a broad absorption spectrum (200–1200 nm) and transforms the absorbed optical energy into heat almost entirely [16, 17]. Stritzker et al. delineated that the temperature of an amelanotic tumor cell suspension enhanced only 3 °C when 808 nm laser irradiated for 2 min, while the temperature of pigmented cells elevated 41 °C under the same conditions [18]. The near-infrared I window (650–950 nm) is absorbed least in normal tissues and penetrates tissue deeply [15]. Therefore, we used an 808 nm laser for PTT to treat MM in mice, followed by subsequent response surveillance studies via ^{18}F-5-FPN and ^{18}F-FDG PET imaging.

Materials And Methods

Synthesis of ^{18}F-5-FPN and ^{18}F-FDG

[18]F-5-FPN was prepared according to our previous protocol in a radiosynthesis module (GE TraceLab FXFN; GE Healthcare, Milwaukee, WI) with radiochemical yields of $7.14 \pm 2.72\%$ (n = 6) and radiochemical purity > 95% [11, 12]. ^{18}F-FDG was obtained (GE-MXFDG, General Electric™, Liege, Belgium) with a radiochemical yield of 70% and radiochemical purity > 98%.

Cell culture

B16F10 (a melanotic MM) and MDA-MB-231 (a breast cancer) cell lines were cultured in the complete medium with Dulbecco's modified Eagle's medium (Gibco™, Carlsbad California, USA), 10% fetal bovine serum (Gibco) and 1% penicillin-streptomycin solution (100 U/mL; Beyotime™, Shanghai, China), and maintained in a humidified incubator containing 5% CO_2 at 37 °C.

Design of animal models

BALB/c nude mice (female, 4 weeks, specific pathogen-free, HFK Bioscience Co., Ltd.™, Beijing, China) were raised under specific pathogen-free facilities with a constant temperature and humidity, and free availability of food and water at 12 h/12 h light/dark cycle, approved by the Laboratory Animal Care of Huazhong University of Science and Technology, and in compliance with the regulations and standards of the Institutional Animal Care and Use Committee of Tongji Medical College of Huazhong University of Science and Technology. All mice adjusted to the new conditions for at least 3 d before an arrangement.

B16F10 (1×10^6) and MDA-MB-231 (5×10^6) cells in 75 μL phosphate buffered saline were subcutaneously injected into the right forelimb of nude mice. B16F10 models for histological analysis were prepared by injecting cells in both forelimbs with one treated and the other untreated. Subsequent studies were carried out when the greatest diameter of the tumors reached approximately 5 mm.

30 µL turpentine was intramuscularly injected in the thigh muscle of the right hindlimb of nude mice served as an inflammatory model. It was followed by ^{18}F-FDG and ^{18}F-5-FPN small animal PET scanning at 24 h and 54 h after injection, respectively [19, 20].

Photothermal therapy (PTT)

B16F10- and MDA-MB-231-xenografted mice were randomized to treated or untreated groups. The treated groups were anesthetized intraperitoneally with 2% pentobarbital sodium solution (80 mg/kg), and placed in the left lateral decubitus position to expose the tumors to the 808 nm laser for 10 min (1 W at a distance of 1.5 cm). During the entire procedure, an IR thermal imaging camera (EasIR-4; Gaode Infrared Limited Company, Wuhan, China) was used to monitor the temperature changes in the tumors continuously. The maximum temperatures were recorded at 20 s intervals in the initial 3 min, followed by 1 min intervals. The day of therapy was termed as Day 0.

PET imaging and analysis

Mice fasted for 6–8 h before ^{18}F-FDG PET acquisition. After mice were anesthetized and placed in the prone position, 10 min static acquisitions were obtained at 1 h after the injection of ^{18}F-FDG (4.11 ± 0.29 MBq) and ^{18}F-5-FPN (4.19 ± 0.29 MBq) via the tail vein.

Quantity analysis was made by Amide software (Amide.exe 1.0.4, SourceForge.net). The whole tumor, inflammatory muscle, and the contralateral normal muscle were manually outlined on the decay-corrected three-dimensional images. The percentage injected dose per gram of tissue (%ID/g) and the uptake ratio of tumor or inflammatory muscle to normal muscle were calculated.

Imaging surveillance of B16F10 models

^{18}F-FDG PET scanning on Day – 2, 1, 5, 8, 16 and ^{18}F-5-FPN PET imaging on Day – 1, 2, 6, 9, 17 were performed on B16F10-xenografted treated and untreated groups (n = 7 per group). Mice were photographed at all imaging time points. If a mouse died during the surveillance or after the last scan, it was dissected to assess whether lung and liver metastases occurred or not, with lung, liver and kidney analyzed via H&E staining.

Comparative imaging of B16F10, inflammatory, and MDA-MB-231 models

B16F10, inflammatory, and MDA-MB-231 mice were prepared for ^{18}F-FDG and ^{18}F-5-FPN PET scans (n = 5 per group). Histological analysis was performed on B16F10 tumor, normal muscle, inflammatory muscle, and MDA-MB-231 tumor after imaging.

Survival analysis

B16F10- and MDA-MB-231-xenografted mice were randomized to treatment or no treatment (n = 10 per group). The treated group was administered PTT protocol. The condition and weight of mice and the tumor size were monitored every other day, and tumor volume was calculated with the formula (length ×

width$^2 \times \pi/6$). If tumor volume was > 2000 mm^3, or if the loss of weight was > 20% of baseline, or if disability of movement, eating, or drinking was observed, mice were euthanized by double 2% pentobarbital sodium solution. Then, the mice were dissected to evaluate whether lung and liver metastases occurred or not.

Histological analysis

B16F10-xenografted tumors in the treated and untreated groups, MDA-MB-231-xenografted tumors, inflamed muscles, normal muscles, lungs, livers, and kidneys were fixed in 4% paraformaldehyde, embedded in paraffin, and cut into 4 µm slices for H&E staining.

Statistical analysis

All quantitative data are expressed as mean ± standard deviation. Two group comparisons were conducted by paired or independent t-tests and multiple group comparisons by one-way analysis of variance (IBM SPSS Statistic 20) with p value < 0.05 representing significance. Kaplan-Meier plots were used to exhibit survival data, and a log-rank test was used to analyze them (GraphPad Prism 6.0 GraphPad Software™, La Jolla, CA, USA).

Results

Photothermal therapy (PTT)

B16F10-xenografted and MDA-MB-231-xenografted mice were irradiated with the 808 nm laser. Over 13 min, an IR thermal imaging camera was used to monitor and record the temperature continuously. The temperature of the B16F10 tumors increased rapidly with the increment of 30 °C in 1 min and finally exceeded 60 °C, while the MDA-MB-231 tumors heated up minimally (< 5 °C) (Fig. 1a, b). The near-infrared images of B16F10 tumor before PTT, and of B16F10 and MDA-MB-231 tumors during PTT, are presented in Fig. 1c. Immediately after PTT, B16F10 tumors appeared smaller, accompanied by a mild circular burn of the surrounding skin due to thermal conduction, while no similar change was found in MDA-MB-231 tumors (Fig. 1d).

Histological analysis of B16F10 tumors

The BALB/c nude mice (n = 5) injected with B16F10 cells in both forelimbs underwent PTT on one side. One day after PTT, both tumors in the treated and untreated sides were collected for H&E staining. Tumors in the untreated group (Fig. 1f) possessed an intact structure and sharp borders. Tumor cells were distributed compactly with visible cellular morphology and brown pigment inside. Conversely, tumors in the treated group (Fig. 1e) showed disordered structure, a large amount of necrosis and pyknosis, and no clear borders. A distinct boundary between the treated and surrounding normal skin on the treated side is shown in Fig. 1g.

Imaging surveillance of B16F10 models

The treated and untreated B16F10-xenografted mice (n = 7 per group) underwent ^{18}F-FDG and ^{18}F-5-FPN PET scans at different set time points (Fig. 2a). Figure 2b depicts the number of surviving mice at each time point. ^{18}F-5-FPN and ^{18}F-FDG images were capable of monitoring the response to PTT in the treated group at different time points (Fig. 2c). Tracer accumulation of tumor sites in the early stage after treatment (Day 1, 2) was lower than before treatment (Day − 2, -1). Although no tumor recurrence was observed in the treated group on Day 5 or 6, PET images showed tracer accumulation at the primary site. On the subsequent scans, tumor relapse was found, with high uptakes. Tumors in the untreated group grew quickly and developed local necrosis, and corresponding ^{18}F-5-FPN and ^{18}F-FDG PET images showed increasing tumor size and initial high uptake followed by an absence of uptake in the necrotic region (Fig. 2d).

Quantitative comparisons among the different groups at different time points are shown in Fig. 2e-h and Table 1. 1) The mean tumor uptakes of ^{18}F-5-FPN in the treated and untreated groups were very high before treatment. In the treated group, uptake dropped initially after treatment, and then slowly increased, while the values in the untreated groups kept on high level first and diminished at the last scan (Fig. 2e). The uptake values of ^{18}F-FDG in the treated and untreated groups were relatively low on the day before treatment, gradually increasing over time in the treated group, while the degree of uptake in the untreated group peaked early and then gradually decreased (Fig. 2f). 2) Comparison between treated and untreated groups on the same day (Fig. 2e, f and Table 1) showed the mean tumor uptakes of ^{18}F-5-FPN and ^{18}F-FDG were similar before treatment (p > 0.05). After treatment, all values differed between the two groups. 3) Values of the tracer uptake before treatment and at each time point after PTT in the treated group are also shown in Fig. 2g, Fig. 2h and Table 1. The mean tumor uptakes of ^{18}F-5-FPN on Day 2 and Day 6 after PTT were much lower than that value before treatment (P < 0.01). However, no significant difference existed between the ^{18}F-FDG uptakes on Day 1 after PTT and before treatment (P > 0.05). Then the tumor recurred and both tracer accumulations increased.

Table 1

^{18}F-5-FPN and ^{18}F-FDG uptakes in both B16F10-xenografted treated and untreated groups at different time points. All data are presented as mean ± standard deviation. (Unit: %ID/g)

^{18}F-5-FPN			^{18}F-FDG		
Day	Treated	Untreated	Treated	Untreated	Day
-1	18.33 ± 4.98	17.82 ± 5.57	6.54 ± 0.84	7.90 ± 1.69	-2
2	7.52 ± 3.65	16.85 ± 3.37	6.18 ± 1.18	16.72 ± 2.76	1
6	10.22 ± 6.00	15.42 ± 2.65	8.69 ± 2.75	15.61 ± 2.06	5
9	17.44 ± 3.08	9.54 ± 2.76	19.02 ± 1.57	11.84 ± 3.15	8
17	17.99 ± 1.81	-	13.50 ± 2.76	-	16

Mice were dissected if they died during the surveillance or were euthanized and then dissected after completion of imaging. Tissue samples of lung, liver and kidney were fixed with 4% paraformaldehyde, embedded, and cut into slices for H&E staining. No lung or liver metastases or renal dysfunction were found (Fig. 3).

Comparative imaging of B16F10, inflammatory and MDA-MB-231 models

Comparative imaging of B16F10-xenografted, inflamed, and MDA-MB-231-xenografted models (n = 5 per group) revealed that only B16F10-xenografted mice had elevated uptake on ^{18}F-5-FPN PET imaging (Fig. 4a2), while ^{18}F-FDG images showed elevated uptake in all three lesions (Fig. 4a3, b3 and c3). In quantitative analysis (Fig. 4d and Table 2), ^{18}F-5-FPN accumulated in B16F10 tumor at 20.36 ± 4.38%ID/g. Uptakes in the MDA-MB-231 tumor and inflammation were significantly lower (p < 0.001). The ^{18}F-5-FPN B16F10 tumor-to-muscle uptake ratio was also substantially higher than that of inflammation-to-healthy muscle and MDA-MB-231 tumor-to-muscle (p < 0.001, Fig. 4e and Table 2). ^{18}F-5-FPN uptakes in inflammatory and healthy sides resembled while higher ^{18}F-FDG values were noted in inflammation than in normal muscle (p < 0.001).

Table 2

[18]F-5-FPN and ^{18}F-FDG values in B16F10-xenografted mice, inflammation-induced mice, and MDA-MB-231-xenografted mice.
All data are presented as mean ± standard deviation.

	^{18}F-5-FPN	^{18}F-FDG
Mean uptake (%ID/g)		
B16F10 Tumor	20.36 ± 4.38	7.06 ± 0.58
Inflammatory Muscle	2.72 ± 0.49	10.31 ± 2.74
Healthy Muscle	2.05 ± 0.46	2.90 ± 0.58
MDA-MB-231 Tumor	1.14 ± 0.30	11.49 ± 3.39
Uptake ratio		
B16F10/Muscle	20.48 ± 7.93	2.45 ± 0.34
Inflammation/Healthy muscle	1.34 ± 0.14	3.57 ± 0.84
MDA-MB-231/Muscle	1.84 ± 0.34	4.02 ± 1.06

After imaging, H&E staining was performed on tissues of interest. B16F10 tumor comprised numerous meganuclear cells with brown pigment inside (Fig. 4f). Muscle fibers in the normal side were arranged orderly and compactly (Fig. 4g1), but those on the inflammatory side were fragmented and separated

with heavy neutrophil infiltration (Fig. 4g2). MDA-MB-231 tumor showed a multitude of plurinuclear cells (Fig. 4h).

Survival analysis

In the survival analysis, B16F10-xenografted and MDA-MB-231-xenografted mice had been randomized to treated and untreated groups. Six days after PTT, B16F10 tumors (n = 10) in the treated group had shrunk dramatically and formed eschar. Then, four mice had no tumor relapsed and only local pigmented dots remained (Fig. 5a "Suppressed" and g "B16F10-Suppressed"). However, tumors of six other treated mice recurred and developed rapidly in a way similar to that in the untreated group (Fig. 5a "Relapse" and g "B16F10-Relapse"). As expected, B16F10 tumors (n = 10) in the untreated group grew rapidly (Fig. 5a "Untreated" and g "B16F10-Untreated"). MDA-MB-231 cells had been subcutaneously injected into twenty nude mice and nineteen tumor models succeeded with one failing. One mouse was excluded due to a large hematoma that interfered with tumor measurement, and so 18 mice were randomized to receive treatment or no treatment. There was no significant difference in tumor size of MDA-MB-231 tumors between treated and untreated groups (Fig. 5d, g "MDA-MB-231-Treated" and "MDA-MB-231-Untreated"). The weights of the B16F10- and MDA-MB-231-xenografted mice in both groups were not significantly different (Fig. 5b, e). The median survivals of B16F10-xenografted suppressed, recurred, and untreated groups were 34, 14.5, and 9.5 days, respectively (p < 0.001). The median survivals of the MDA-MB-231-xenografted treated and untreated groups were 29 and 30 days, respectively (p > 0.05). No mice had lung or liver metastases at the monitoring end point.

Discussion

Our research used an 808 nm laser to treat B16F10 tumors engrafted into nude mice. We explored the feasibility of ^{18}F-5-FPN PET imaging for PTT response evaluation, further compared with the detection of inflammation and other tumors to ascertain its specificity for MM. ^{18}F-5-FPN is a promising probe to assess the therapeutic response of MM and is likely to be a new strategy for the clinical response evaluation and follow-up of MM.

[18]F-5-FPN and ^{18}F-FDG PET acquisitions were performed on B16F10- engrafted models in treated and untreated groups at each time point (Fig. 2a). In the treated group (Fig. 2c), tracer accumulation in tumors after PTT (Day 1, 2) declined from baseline. No recurrence was discovered via gross inspection within 6 days after treatment. Nevertheless, regional uptakes were observed clearly on Day 5 and 6 in mice. Then the tumor relapsed with corresponding tracer accumulation. Hence, ^{18}F-5-FPN PET imaging might help to reveal an occult residual recurrence before observation.

Tumor cells were killed by PTT and tumor size shrank. Residual tumor cells regrew and tumor relapsed later. In the quantitative analysis of images (Fig. 2g, h and Table 1), the mean tumor uptakes of ^{18}F-5-FPN in the treated group declined on Day 2 and 6, then enhanced, which represented the diminution of melanin in tumor tissue after PTT followed by escalation. Serial ^{18}F-5-FPN PET imaging recorded the

course accurately with high sensitivity. No difference was found for ^{18}F-FDG uptake before and on Day 1 after therapy, implying less sensitivity compared to ^{18}F-5-FPN. Therefore, ^{18}F-5-FPN might have a higher sensitivity to an early response.

In the untreated group, tumor size was small initially with low ^{18}F-FDG uptake and enlarged gradually with increasing ^{18}F-FDG uptake, while ^{18}F-5-FPN values remained on a high level. Although the mean tumor uptakes attenuated due to local necrosis later, the maximum uptakes of the whole tumor were still high (Day 9, ^{18}F-5-FPN, 35.92 ± 5.61%ID/g. Day 8, ^{18}F-FDG, 29.16 ± 5.53% ID/g).

CT and MRI are generally used to evaluate therapy response in the clinic. However, they sometimes fail to discriminate between real progression and pseudoprogression. One investigation revealed that 22 out of 227 patients responded atypically, and lesions were confirmed to be inflammatory infiltration and necrosis, not tumor proliferation by biopsy [7]. Moreover, conventional techniques cannot monitor tumor response to immunotherapy in a timely and accurate fashion [6, 8]. The previous article reported that the pseudoprogression rate via conventional techniques was as high as 10–15% for malignant melanoma patients treated with immunotherapy [21]. Changes in tumor function and metabolism always precede changes in size. Thus, functional imaging may facilitate the detection of early therapy response [7, 22, 23].

By now, a few probes have been explored for early diagnosis or staging of MM, but few potential agents have been evaluated for response evaluation, except for [18]F−FDG and ^{18}F-FLT [6−8, 13, 14]. ^{18}F-FDG PET/CT imaging plays an important role in response evaluation to conventional chemotherapy, and also has some value in targeted therapy and immunotherapy [7, 8]. Geven et al. used ^{18}F-FDG and ^{18}F-FLT PET imaging to assess the response of MM models to BRAF-mutant inhibitor and revealed that tumor uptakes of ^{18}F-FLT had no difference before and after therapy, though the accumulation of ^{18}F-FDG decreased obviously after therapy [13]. Because both MM and immune-related inflammation accumulate ^{18}F-FDG, ^{18}F-FDG PET imaging may make it quite challenging to differentiate between real progression and pseudoprogression [7]. One study investigated 12 metastatic MM patients under anti-CTLA-4 antibody treatment. It concluded that the SUV_{max} changes of ^{18}F-FDG and ^{18}F-FLT PET images would not offer reliable value to predict late response 3 months after the first therapy [14]. However, another article concluded that early ^{18}F-FDG PET/CT scanning could predict the response of MM to immunotherapy [6]. According to the literature, it is still controversial whether ^{18}F-FDG PET imaging might estimate therapy response of MM well or not, and whether the imaging can exclude the interference of inflammation and detect an occult residual recurrence efficiently in the clinic.

Similarly, in our imaging surveillance, the area of ^{18}F-FDG accumulation was larger than that of ^{18}F-5-FPN on Day 1 vs. Day 2 and Day 5 vs. Day 6 (Fig. 2c). Comparative imaging of B16F10 tumor, inflammation and MDA-MB-231 tumor was subsequently implemented to judge whether inflammation might affect the result or not.

In the comparative imaging, only B16F10 tumor was distinctly visible on ^{18}F-5-FPN PET imaging, while three models were all obvious on ^{18}F-FDG PET images (Fig. 4a-c). Quantitative analysis also corroborated that B16F10 tumor accumulated considerable ^{18}F-5-FPN, and all three showed high uptakes of ^{18}F-FDG (Fig. 4d and Table 2). Moreover, ^{18}F-5-FPN uptakes of inflammatory and healthy sides resembled, while inflammation accumulated much more ^{18}F-FDG than normal muscle. ^{18}F-5-FPN displays an excellent affinity for melanin, but the specificity of ^{18}F-FDG is not good enough to distinguish between tumor and inflammation, nor between pigmented tumors and other carcinomas. Local inflammation may emerge after PTT, and ^{18}F-FDG cannot reveal early response to therapy accurately. This may be correlated to the finding that ^{18}F-5-FPN uptake declined early after PTT, while a reduction in ^{18}F-FDG uptake was not obvious in this research (Fig. 2g, h). Here, the smaller size of the B16F10 tumor may be responsible for its lower uptake of ^{18}F-FDG than that of the other two models. This can also be demonstrated by the value > 13%ID/g over the increasing volume of B16F10 tumor in the imaging surveillance.

The therapy landscape of MM has made profound progress and several drugs for targeted therapy and immunotherapy, including vemurafenib, dabrafenib, ipilimumab, pembrolizumab, and nivolumab, have been approved following clinical trials [2]. Overall, targeted therapy achieves short-term palliation, immunotherapy needs a long time to judge the response, and the two approaches induce different kinds of side effects [2–5, 24]. Thereby, this research did not adopt drug therapy but PTT. Exposed to an 808 nm laser, the temperature of B16F10 tumors increased rapidly [15, 25–28], but only slightly in MDA-MB-231 tumors. Melanin can transform optical energy into heat efficiently. Histological analysis, imaging surveillance, and survival analysis identified that the PTT protocol inhibited tumor growth strikingly over a short time, although all tumors eventually recurred. It said that tumor cells might tolerate hyperthermia via the mediation of heat shock proteins to enhance their survival rate, which might explain why tumors relapsed after PTT [29]. Thus, several reports have explored gold nanomaterials or other materials to improve the efficacy of PTT and even combined PTT with chemotherapy or other treatment strategies [15, 25–27, 30–35].

The melanin in MM successfully transformed light energy into heat for PTT. Tumor growth was suppressed for a short time, and ^{18}F-5-FPN PET imaging was more sensitive to estimate the early response of B16F10 tumor to PTT than ^{18}F-FDG. Unfortunately, tumors recurred later. Prior to observation, ^{18}F-5-FPN and ^{18}F-FDG PET imaging detected occult residual recurrence. Moreover, ^{18}F-5-FPN showed high specificity for MM and overcame the interference of inflammation, suggesting a more accurate response evaluation. Undoubtedly, the superiority of ^{18}F-5-FPN may offer a new approach for MM response assessment and follow-up. This research still has some limitations. 1) PTT can only be used for superficial lesions and cannot work for deep or visceral metastatic lesions. Therefore, our group plans to assess therapy response of a metastatic model of human MM cell line to targeted therapy or immunotherapy via ^{18}F-5-FPN PET imaging. 2) Although > 90% of primary cases are pigmented [36, 37], a minority of MMs are amelanotic, making them unsuitable for ^{18}F-5-FPN PET imaging.

Conclusions

^{18}F-5-FPN PET imaging successfully evaluated the early therapy response of MM, detected occult residual recurrence after PTT, and further confirmed the close affinity with melanin by distinguishing MM from inflammation and other carcinomas. This potential probe may provide a new strategy for MM patients by means of efficient response evaluation.

Abbreviations

MM: Malignant melanoma;

PTT: Photothermal therapy;

PET: Positron-emission tomography;

^{18}F-5-FPN: ^{18}F-5-fluoro-N-(2-(diethylamino)ethyl)picolinamide;

^{18}F-FDG: ^{18}F-fluorodeoxyglucose;

H&E: Hematoxylin and eosin;

CT: Computed tomography;

MRI: Magnetic resonance imaging;

PD-1: Programmed death 1;

^{18}F-FLT: ^{18}F-fluorothymidine;

CTLA-4: cytotoxic T lymphocyte–associated antigen 4.

Declarations

Acknowledgments

Authors' contributions

Funding

Availability of data and materials

The datasets obtained and analyzed during the current study were made available from the corresponding authors through request.

Ethics approval

All procedures performed in studies involving animals were in accordance with the ethical standards of the Institutional Animal Care and Use Committee of Tongji Medical College of Huazhong University of Science and Technology.

Consent for publication

Consent to publish has been obtained from all authors.

Competing interests

The authors declare that they have no competing interests.

References

1. Karimkhani C, Green AC, Nijsten T, Weinstock MA, Dellavalle RP, Naghavi M, Fitzmaurice C. The global burden of melanoma: results from the Global Burden of Disease Study 2015. Br J Dermatol. 2017; 177: 134-40.
2. Luke JJ, Flaherty KT, Ribas A, Long GV. Targeted agents and immunotherapies: optimizing outcomes in melanoma. Nat Rev Clin Oncol. 2017; 14: 463-42.
3. Luke JJ, Schwartz GK. Chemotherapy in the management of advanced cutaneous malignant melanoma. Clin Dermatol. 2013; 31: 290-7.

4. Karimkhani C, Reddy BY, Dellavalle RP, Sundararajan S. Novel therapies for unresectable and metastatic melanoma. BMJ. 2017; 359: j5174.

5. Long GV, Stroyakovskiy D, Gogas H, Levchenko E, Braud F, Larkin J, Garbe C, Jouary T, Hauschild A, Grob JJ, et al. Combined BRAF and MEK inhibition versus BRAF inhibition alone in melanoma. N Engl J Med. 2014; 371: 1877-88.

6. Sachpekidis C, Larribere L, Pan L, Haberkorn U, Dimitrakopoulou-Strauss A, Hassel JC. Predictive value of early 18F-FDG PET/CT studies for treatment response evaluation to ipilimumab in metastatic melanoma: preliminary results of an ongoing study. Eur J Nucl Med Mol Imaging. 2015; 42: 386-96.

7. Wong ANM, McArthur GA, Hofman MS, Hicks RJ. The Advantages and Challenges of Using FDG PET/CT for Response Assessment in Melanoma in the Era of Targeted Agents and Immunotherapy. Eur J Nucl Med Mol Imaging. 2017; 44: 67-77.

8. Gilles R, Geus-Oei LF, Mulders PF, Oyen WJ. Immunotherapy response evaluation with (18)F-FDG-PET in patients with advanced stage renal cell carcinoma. World J Urol. 2013; 31: 841-6.

9. Kong BY, Menzies AM, Saunders CA, Liniker E, Ramanujam S, Guminski A, Kefford RF, Long GV, Carlino MS. Residual FDG-PET metabolic activity in metastatic melanoma patients with prolonged response to anti-PD-1 therapy. Pigment Cell Melanoma Res. 2016; 29: 572-7.

10. Wei WJ, Ehlerding EB, Lan XL, Luo QM, Cai WB. PET and SPECT imaging of melanoma: the state of the art. Eur J Nucl Med Mol Imaging. 2018; 45: 132-50.

11. Feng HY, Xia XT, Li CJ, Song YL, Qin CX, Liu QY, Zhang YX, Lan XL. Imaging malignant melanoma with (18)F-5-FPN. Eur J Nucl Med Mol Imaging. 2016; 43: 113-22.

12. Wang YC, Li MT, Zhang YY, Zhang FZ, Liu CB, Song YL, Zhang YX, Lan XL. Detection of melanoma metastases with PET-Comparison of 18F-5-FPN with 18F-FDG. Nucl Med Biol. 2017; 50: 33-8.

13. Geven EJ, Evers S, Nayak TK, Bergström M, Su F, Gerrits D, Franssen GM, Boerman OC. Therapy response monitoring of the early effects of a new BRAF inhibitor on melanoma xenograft in mice: evaluation of (18) F-FDG-PET and (18) F-FLT-PET. Contrast Media Mol Imaging. 2015; 10: 203-10.

14. Ribas A, Benz MR, Allen-Auerbach MS, Radu C, Chmielowski B, Seja E, Williams JL, Gomez-Navarro J, McCarthy T, Czernin J. Imaging of CTLA4 blockade-induced cell replication with (18)F-FLT PET in patients with advanced melanoma treated with tremelimumab. J Nucl Med. 2010; 51: 340-6.

15. Vijayaraghavan P, Liu CH, Vankayala R, Chiang CS, Hwang KC. Designing multi-branched gold nanoechinus for NIR light activated dual modal photodynamic and photothermal therapy in the second biological window. Adv Mater. 2014; 26: 6689-95.

16. Meredith P, Sarna T. The physical and chemical properties of eumelanin. Pigment Cell Res. 2006; 19: 572-94.

17. Anderson RR, Parrish JA. Selective photothermolysis: precise microsurgery by selective absorption of pulsed radiation. Science. 1983; 220: 524-7.

18. Stritzker J, Kirscher L, Scadeng M, Deliolanis NC, Morscher S, Symvoulidis P, Schaefer K, Zhang Q, Buckel L, Hess M, et al. Vaccinia virus-mediated melanin production allows MR and optoacoustic

deep tissue imaging and laser-induced thermotherapy of cancer. Proc Natl Acad Sci USA. 2013; 110: 3316-20.

19. Niu G, Lang L, Kiesewetter DO, Ma Y, Sun Z, Guo N, Guo J, Wu C, Chen X. In Vivo Labeling of Serum Albumin for PET. J Nucl Med. 2014; 55: 1150-6.

20. Liu Z, Chen H, Chen K, Shao Y, Kiesewetter DO, Niu G, Chen X. Boramino acid as a marker for amino acid transporters. Sci Adv. 2015;1: e1500694.

21. Hodi FS, Hwu WJ, Kefford R, Weber JS, Daud A, Hamid O, Patnaik A, Ribas A, Robert C, Gangadhar TC, et al. Evaluation of Immune-Related Response Criteria and RECIST v1.1 in Patients with Advanced Melanoma Treated with Pembrolizumab. J Clin Oncol. 2016; 34: 1510-7.

22. Barrington SF, Mikhaeel NG, Kostakoglu L, Meignan M, Hutchings M, Müeller SP, Schwartz LH, Zucca E, Fisher RI, Trotman J, et al. Role of imaging in the staging and response assessment of lymphoma: consensus of the International Conference on Malignant Lymphomas Imaging Working Group. J Clin Oncol. 2014; 32: 3048-58.

23. Mottok A, Steidl C. Biology of classical Hodgkin lymphoma: implications for prognosis and novel therapies. Blood. 2018; 131: 1654-65.

24. Thompson JF, Scolyer RA, Kefford RF. Cutaneous melanoma. Lancet. 2005; 365: 687-701.

25. Coughlin AJ, Ananta JS, Deng N, Larina IV, Decuzzi P, West JL. Gadolinium-conjugated gold nanoshells for multimodal diagnostic imaging and photothermal cancer therapy. Small. 2014; 10: 556-65.

26. Lu W, Melancon MP, Xiong C, Huang Q, Elliott A, Song S, Zhang R, Flores LG, Gelovani JG, Wang LV, et al. Effects of photoacoustic imaging and photothermal ablation therapy mediated by targeted hollow gold nanospheres in an orthotopic mouse xenograft model of glioma. Cancer Res. 2011; 71: 6116-21.

27. Heidari M, Sattarahmady N, Azarpira N, Heli H, Mehdizadeh AR, Zare T. Photothermal cancer therapy by gold-ferrite nanocomposite and near-infrared laser in animal model. Lasers Med Sci. 2016; 31: 221-7.

28. Habash RW, Bansal R, Krewski D, Alhafid HT. Thermal therapy, part 1: an introduction to thermal therapy. Crit Rev Biomed Eng. 2006; 34: 459-89.

29. Li YY, Jiang CH, Zhang DW, Wang Y, Ren XY, Ai KL, Chen XS, Lu LH. Targeted polydopamine nanoparticles enable photoacoustic imaging guided chemo-photothermal synergistic therapy of tumor. Acta Biomater. 2017; 47: 124-34.

30. Zhang PC, Hu CH, Ran W, Meng J, Yin Q, Li YP. Recent Progress in Light-Triggered Nanotheranostics for Cancer Treatment. Theranostics. 2016; 6: 948-68.

31. Jin HL, Zhao GF, Hu JL, Ren QG, Yang K, Wan C, Huang A, Li PD, Feng JP, Chen J, et al. Melittin-Containing Hybrid Peptide Hydrogels for Enhanced Photothermal Therapy of Glioblastoma. ACS Appl Mater Interfaces. 2017; 9: 25755-66.

32. Liu YX, Li LY, Guo QW, Wang L, Liu DD, Wei ZW, Zhou J. Novel Cs-Based Upconversion Nanoparticles as Dual-Modal CT and UCL Imaging Agents for Chemo-Photothermal Synergistic Therapy.

Theranostics. 2016; 6: 1491-05.

33. Zhang W, Guo ZY, Huang DQ, Liu ZM, Guo X, Zhong HQ. Synergistic effect of chemo-photothermal therapy using PEGylated graphene oxide. Biomaterials. 2011; 32: 8555-61.

34. Zhang LW, Rong PF, Chen ML, Gao S, Zhu L. A novel single walled carbon nanotube (SWCNT) functionalization agent facilitating in vivo combined chemo/thermo therapy. Nanoscale. 2015; 7: 16204-13.

35. Bear AS, Kennedy LC, Young JK, Perna SK, Mattos Almeida JP, Lin AY, Eckels PC, Drezek RA, Foster AE. Elimination of metastatic melanoma using gold nanoshell-enabled photothermal therapy and adoptive T cell transfer. PLoS One. 2013; 8: e69073.

36. Chezal JM, Papon J, Labarre P, Lartigue C, Galmier MJ, Decombat C, Chavignon O, Maublant J, Teulade JC, Madelmont JC. Evaluation of radiolabeled (hetero)aromatic analogues of N-(2-diethylaminoethyl)-4-iodobenzamide for imaging and targeted radionuclide therapy of melanoma. J Med Chem. 2008; 51: 3133-44.

37. Eisenhut M, Hull WE, Mohammed A, Mier W, Lay D, Just W, Gorgas K, Lehmann WD, Haberkorn U. Radioiodinated N-(2-diethylaminoethyl)benzamide derivatives with high melanoma uptake: structure-affinity relationships, metabolic fate, and intracellular localization. J Med Chem. 2000; 43: 3913-22.
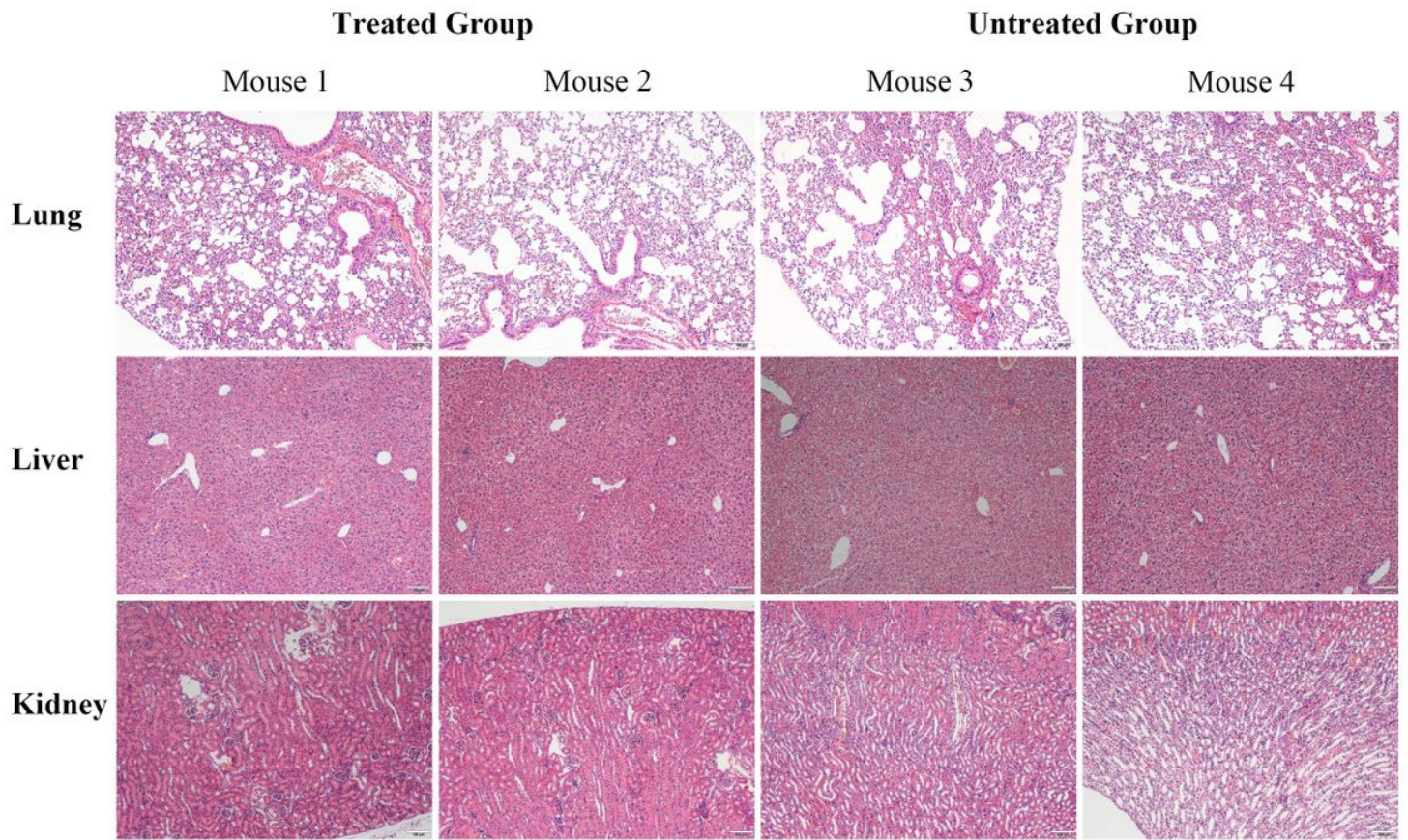
Figures
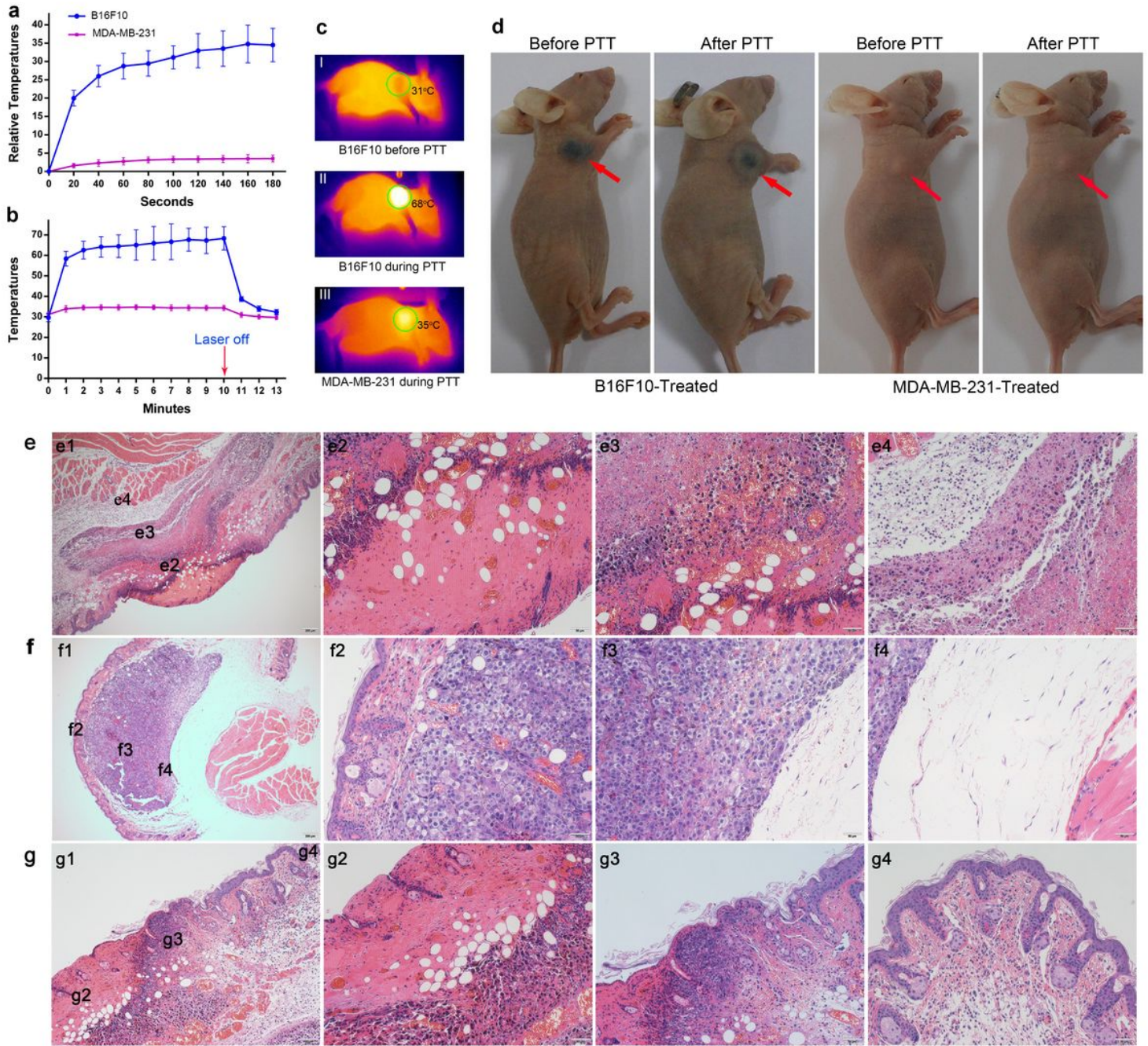
Figure 1

PTT was performed on B16F10- and MDA-MB-231-xenografted mice. (a) Temperature increments in B16F10 and MDA-MB-231 tumors in the initial 3 min of PTT. (b) Temperature changes of B16F10 and MDA-MB-231 tumors over the whole 13-min procedure. (c) IR thermal images of B16F10 and MDA-MB-231 tumors at different times. (d) Photographs of both tumors before and immediately after PTT (red arrows). H&E staining of B16F10 tumors in the treated (e, g) and untreated (f) groups. (g) Clear boundary between the irradiated region and surrounding normal skin in the B16F10-xenografted treated group, with loss of the primary structure and extensive necrosis and pyknosis with some sebaceous glands remaining in the visual field. Bars, e1 and f1-200 µm, g1-100 µm, others-50 µm.
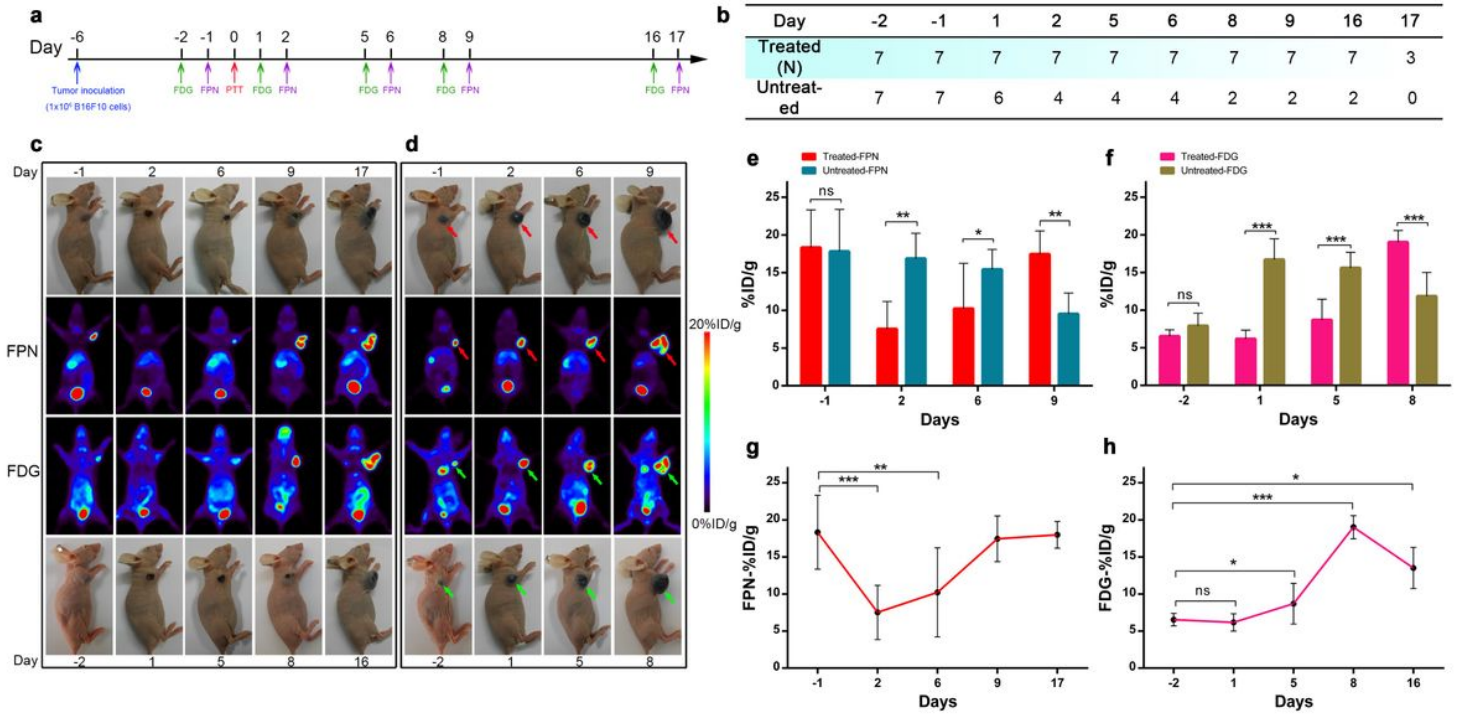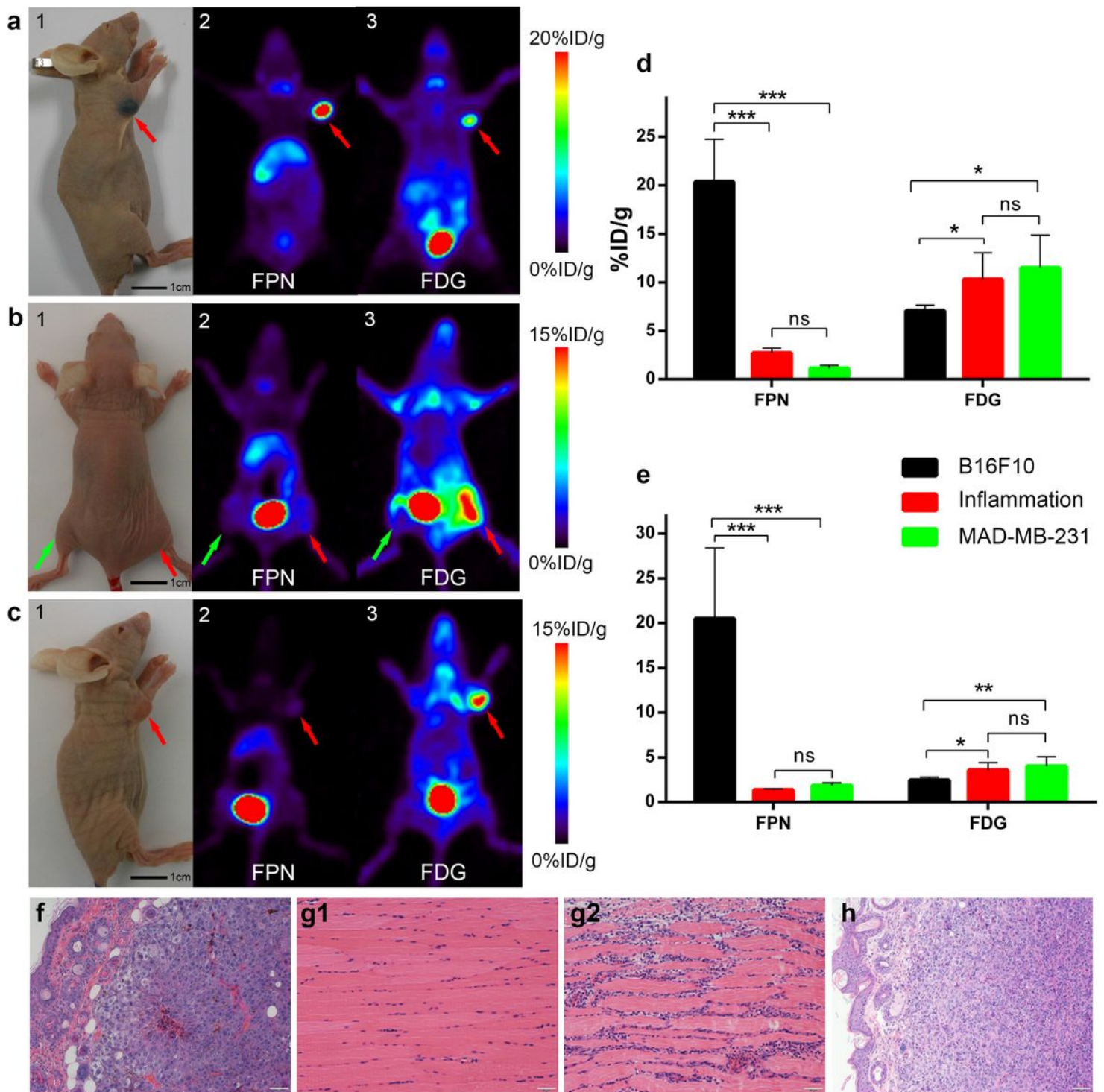
Figure 2

18F-5-FPN and 18F-FDG PET imaging surveillance of B16F10-xenografted mice in treated and untreated groups. (a) The scheme of imaging surveillance. (b) Number of living mice in each group at every time point. 18F-5-FPN and 18F-FDG images and corresponding photographs in the treated (c) and untreated (d) groups, respectively. (e) and (f) show the mean tumor uptakes of 18F-5-FPN and 18F-FDG. (g) and (h) compare the tumor uptakes in the treated mice before and after PTT. Ns, no significance, *p < 0.05, **p < 0.01, ***P < 0.001.
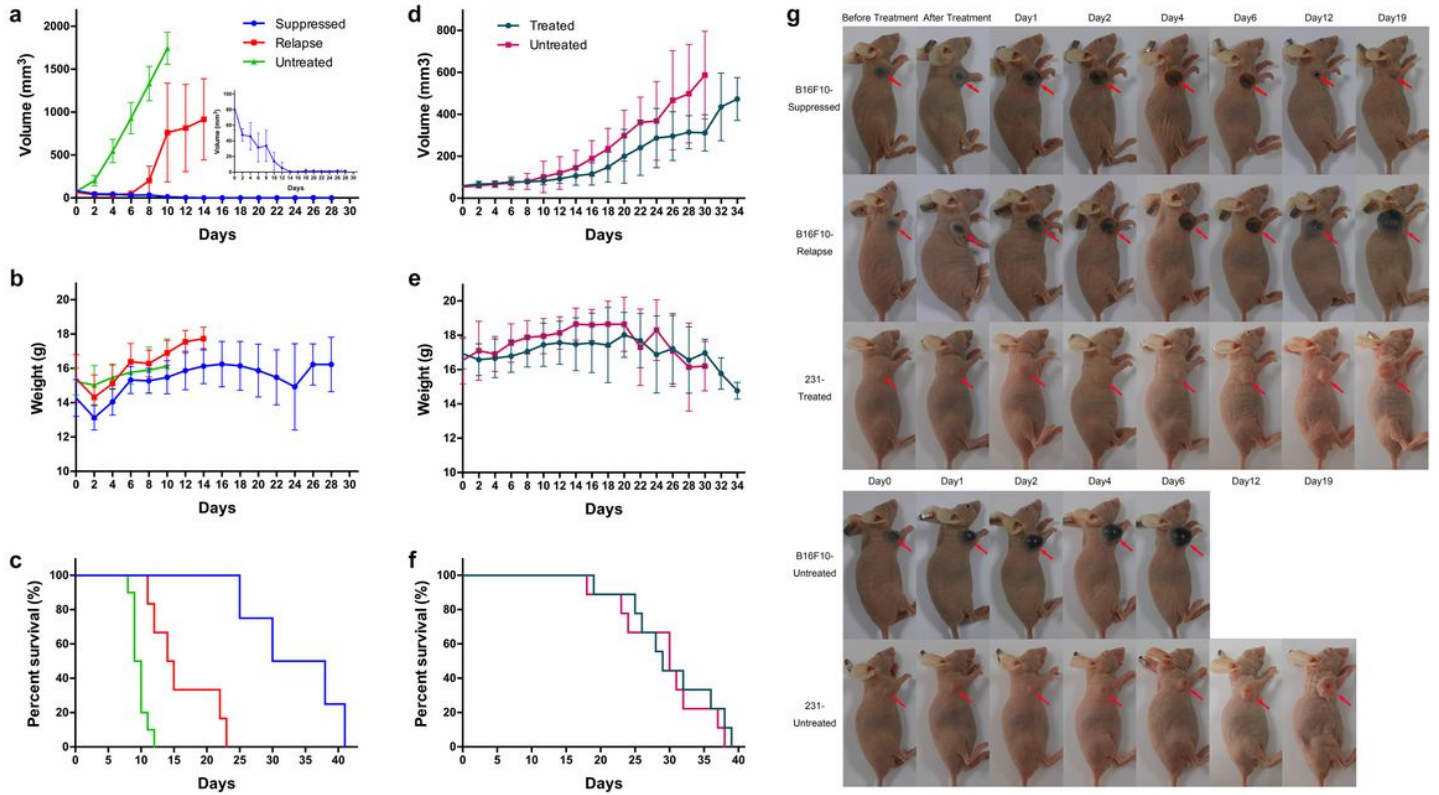
Figure 3

H&E staining of lung, liver and kidney in treated group and untreated group. (Bars, 100 μm)

Figure 4

Comparative imaging and microscope photos of different animal models. Light photographs (1), 18F-5-FPN PET images (2) and 18F-FDG PET images (3) of B16F10 tumor model (a), inflammatory model (b), and MDA-MB-231 tumor model (c). Mean uptakes of 18F-5-FPN and 18F-FDG in the three models (d). Tumor-to-muscle ratios and inflammation-to-normal muscle ratios of 18F-5-FPN and 18F-FDG in the three models (e). H&E staining of B16F10 tumor (f), normal muscle (g1), inflamed muscle (g2), and MDA-MB-231 tumor (h). Bars, 50 μm. Ns, no significance, *p < 0.05, **p < 0.01, ***p < 0.001.

Figure 5

Survival analysis of B16F10- and MDA-MB-231 -xenografted mice. Tumor volume, body weight and Kaplan-Meier survival plot of different groups in B16F10 models (a, b, c) and MDA-MB-231 models (d, e, f), respectively. (g) Tumor changes (red arrows) of B16F10- and MDA-MB-231-xenografted mice in the treated and untreated groups at different days.